Coupled Systems Mechanics, *Vol. 5, No. 4 (2016) 329-340*
DOI: https://doi.org/10.12989/csm.2016.5.4.329

The observation of microstructures in the trigonal shape memory alloys

Tzu-Cheng Liu[a] and Nien-Ti Tsou[*]

Department of Materials Science and Engineering, NCTU, Ta Hsueh Road, HsinChu 300, Taiwan

(Received June 6, 2015, Revised December 10, 2015, Accepted December 15, 2015)

Abstract. The trigonal shape memory alloys (SMAs) have a great potential to be utilized as the applications with special purposes, such as actuators with high operation frequency. Most studies on the trigonal microstructures typically focus on the well-known classic herringbone pattern, but many other patterns are also possible, such as non-classic herringbone, toothbrush and checkerboard patterns. In the current work, a systematic procedure is developed to find all possible laminate twin microstructures by using geometrically linear compatibility theory. The procedure is verified by SEM images with the information of crystallographic axes of unitcells obtained by EBSD, showing good agreement. Many interesting trigonal R-phase patterns are found in the specimen. Then, their incompatibility are analyzed with nonlinear compatibility theory. The relationship between such incompatibility and the likelihood of occurrence of the microstructures is revealed. The current procedure is rapid, computationally efficient and sufficiently general to allow further extension to other crystal systems and materials.

Keywords: shape memory alloys; compatibility; laminate twins

1. Introduction

Shape memory alloys (SMAs) have been widely used for industrial applications such as sensors and actuators. The trigonal R-phase actuators are useful due to their high operation frequency and small temperature hysteresis (Miyazaki 1999, Tomozawa 2006). Trigonal R-phase which has high internal friction compared to the other crystal systems, is also suitable for high damping applications (Fan 2006). The trigonal SMAs have a great potential for the applications with special purposes. The origin of these special properties mentioned above is the formation of microstructures. While most studies focus on the microstructures in the monoclinic or orthorhombic crystal system, there are fewer researches related to trigonal R-phase. This motivates the current study. We focus on the theoretical calculation for the trigonal microstructures and their stable states. The calculation is helpful for the internal mechanical analysis of microstructures, such as stress distribution and defects.

Observations show that the microstructures in SMAs typically form laminated twins (Bhattacharya 2003). The twin patterns form based on the constrained theory (Ball 1989) in order

*Corresponding author, Assistant Professor, E-mail: tsounienti@nctu.edu.tw
[a]Graduate Student, E-mail: jasoin79121400@hotmail.com

Copyright © 2016 Techno-Press, Ltd.
http://www.techno-press.org/?journal=csm&subpage=8 ISSN: 2234-2184 (Print), 2234-2192 (Online)

to minimize the energy. The theory reveals the importance of the compatible interface separating different variants or phases. There are many studies related to the compatibility theories (Hane 1999, Hane 2000, Tsou 2012). They can be classified into two types: geometrically linear theory and nonlinear theory. The former assumes that the unit cell distortion is small during the phase transformation, and neglects the rigid body rotations between unit cells. The latter considers the rigid body rotations between variants and the nonlinearity of the phase transformation. Nonlinear theory is more restrictive, and therefore, certain microstructures, which are found in geometrically linear theory, are not feasible in the nonlinear theory.

There are various numerical methods to seek the compatible microstructures in SMAs. Molecular dynamics (MD) predict the alignment of atoms under loads showing the evolution of the microstructure in detail (Kastner 2011, Murakami 2007, Zhong 2012). Phase field method is a main numerical method to simulate twin patterns by using Ginzburg-Landau (TDGL) equations and the order parameters (Levitas 2004, Shu 2007, 2008, Zhang 2005). Shu (2007) successfully predicted twin patterns of herringbone and other periodic topologies in the Ni-Ti alloys. Wu (2008) simulated the evolution of strain and martensite microstructure during compressive stress loading and unloading. Although MD and phase field method can provide the information in detail, they generally require cumbersome calculations. Thus, these methods can't apply to the large region in SMAs. By contrast, the sharp interface approaches (Goldsztein 2001, Roytburd 1998, Tsou 2012) treat the interface separating distinct variants as a discontinuity and assume the twin patterns as laminates, saving a great amount of computation. These approaches are suitable for overall and rapid searching for compatible twin patterns.

The "herringbone" twins are the most commonly observed microstructures. They are self-accommodating twins, and typically regarded as multi-rank laminates which will be discussed in more detail in Sec. 2.1. This type of twins has been widely studied both computationally and experimentally. However, the observations for the other types of topology in the trigonal crystal system, such as toothbrush, checkboard and non-symmetric herringbone, are also possible. These twin patterns can be predicted by the geometrically linear compatibility, but unable to be found by the non-linear compatibility theory. This indicates that the classification of microstructures should be based on the geometrically linear compatibility theory, while the defect and detailed incompatibility in the microstructures should be examined by the non-linear compatibility theory.

In this work, an iteration procedure (which will be described in more detail in Sec 2.4) to search, identify and analyze twin patterns in the trigonal SMAs observed by SEM and EBSD, is developed. The iteration method requires detailed construction of the 3-dimensional geometry of the microstructure and proper rotation operations to the geometry to visualize the observation plane revealing the twin patterns. The twin patterns are then classified based on the microstructure database, which generated by the method developed previously by the authors (Tsou 2015). Thus, the likelihood of occurrence of these twin patterns can be further examined and correlated with their incompatibility determined by non-linear compatibility theory. The procedure is rapid, computationally efficient and sufficiently general to allow further extension to other crystal systems and materials.

2. Theory and methodology

2.1 Tree diagram

In the trigonal SMAs, there are four variants with the strain state $\varepsilon_{(i)}$, (i=1...4)

$$\boldsymbol{\varepsilon}_{(1)} = \begin{bmatrix} \alpha & \delta & \delta \\ \delta & \alpha & \delta \\ \delta & \delta & \alpha \end{bmatrix}, \boldsymbol{\varepsilon}_{(2)} = \begin{bmatrix} \alpha & -\delta & -\delta \\ -\delta & \alpha & \delta \\ -\delta & \delta & \alpha \end{bmatrix},$$
$$\boldsymbol{\varepsilon}_{(3)} = \begin{bmatrix} \alpha & \delta & -\delta \\ \delta & \alpha & -\delta \\ -\delta & -\delta & \alpha \end{bmatrix}, \boldsymbol{\varepsilon}_{(4)} = \begin{bmatrix} \alpha & -\delta & \delta \\ -\delta & \alpha & -\delta \\ \delta & -\delta & \alpha \end{bmatrix} \tag{1}$$

where a and δ are the material properties. In the laminate twins, pure variants can be regarded as rank-0 laminations, and a pair of the rank-0 lamination can be combined as a rank-1 lamination, and so on so forth. Thus, a hierarchical binary tree diagram can illustrate the arrangement of a rank-R laminate twins. Since it is difficult to form an exactly compatible laminate with rank higher than 2, most observed microstructures in SMAs are composition of many laminates of rank-2 and lower. Thus, only the laminate microstructures with rank lower than 2 are considered in the present work.

Fig. 1 shows the tree diagram representing a rank-2 lamination. A top-down numbering of the nodes is used. The first node (root node), at the top level of the tree, represents the entire laminate. Nodes at lower levels in the tree represent structures that are combined to form higher rank laminations. At the lowest level, the nodes represent pure crystal variants. For example, the entire rank-2 laminate represented by Node 1 is named "1314". Similarly, the rank-1 laminate represented by Node 2 is labeled "13". The binary tree diagram contains seven nodes i(i=1...7) and each node has its volume fraction f_i and average strain state ε_i. Each parent node has a volume fraction equal to the sum of those of its child nodes: $f_i=f_{2i}+f_{2i+1}$. Similarly, parent nodes have an average strain state derived from those of its child nodes: $\varepsilon_i=f_{2i}\boldsymbol{\varepsilon}_{2i}+f_{2i+1}\boldsymbol{\varepsilon}_{2i+1}$. The rank-1 interface of Node 2 with interface normal n_2 separates variant 1, 3 and the interface of Node 3 with interface normal n_3 separates variant 1, 4. The rank-2 interface of Node 1 with interface normal n_1 separates two regions of rank-1 laminate twins.

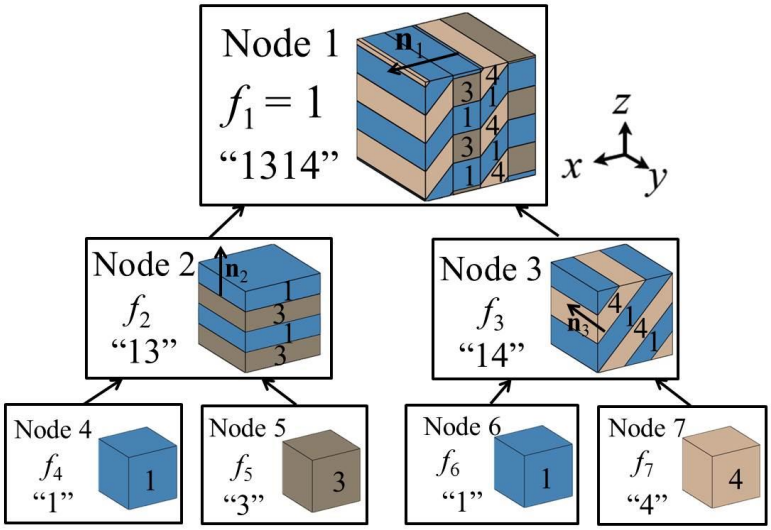

Fig. 1 A binary tree for rank-2 laminate twins of "1314"

Now consider all possible rank-2 laminate microstructure. There are four nodes in the lowest level and each node can represent one of the variants 1…4. This gives 4^4=256 possible variant permutations for the trigonal crystal system. In order to reduce the amount of the computation, mutually equivalent variant permutations should be eliminated. Some of the variant permutations produce the identical relative position of variants in the tree diagram. For example, the permutation 1314 is equivalent to the permutations 1413, 3141 and 4131. After the elimination, the amount of permutations decreased from 256 to 77. These permutations will be examined by the compatibility theory in the next section.

2.2 Geometrically linear compatibility theory and the compatibility conditions

Consider a pair of rank-0 or rank-1 laminate *i*, *j* with average strain states ε_i, ε_j. A compatible interface with unit normal vector *n* satisfies the well-known compatibility equation

$$\boldsymbol{\varepsilon}_j - \boldsymbol{\varepsilon}_i = \frac{1}{2}(\mathbf{a} \otimes \mathbf{n} + \mathbf{n} \otimes \mathbf{a}) \tag{2}$$

where *a* is an arbitrary vector. Eq. (2) can be solved by using the eigenvalues λ_k (k=1…3) and eigenvectors e_k of the 3×3 matrix $M=\varepsilon_j - \varepsilon_i$. Generally, two solutions of the compatible interface normal can be found whenever $\lambda_1 = -\lambda_3$ and $\lambda_2 = 0$, giving

$$\mathbf{n} = \frac{\pm\sqrt{-\lambda_1/\lambda_3}\,\mathbf{e}_1 + \mathbf{e}_3}{\sqrt{1-\lambda_1/\lambda_3}} = \frac{\mathbf{e}_3 \pm \mathbf{e}_1}{\sqrt{2}} \tag{3}$$

Since each node has two solutions of the interface *n* and there are three nodes with interface in a rank-2 tree diagram, a permutation can produce $2^3=8$ distinct laminate twin microstructure at most. Continuing the Sec. 2.1, there are 77 variant permutations in trigonal crystal system. Thus, there are in total 77×8=616 sets of distinct laminate twin microstructure.

However, not all combinations of the trigonal variants can form compatible laminate twin patterns. A compatible rank-2 laminate is required to satisfy the three exact compatibility conditions (Tsou 2010): (i) Interfaces between the distinct phases must have the same spacing wherever they meet at any higher level interface. This means that the volume fraction ratio of child nodes should be identical, i.e., $f_4/f_5=f_6/f_7$. (ii) The interface normals of any two nodes and their parent node that connect them must be coplanar, i.e., the interface normal of Node 1, 2, 3 should satisfy $n_1 \cdot (n_2 \times n_3)=0$. (iii) Wherever two phases meet, their interface in the crystal must satisfy Eq. (2), i.e., Node 4 and Node 5 must be compatible across the interface with normal n_2; Node 4 and Node 6 must be compatible across the interface with normal n_1.

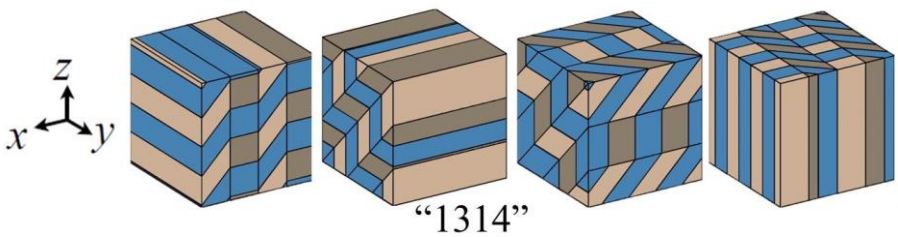

Fig. 2 Four different laminate twin microstructures produced from the variant permutation 1314

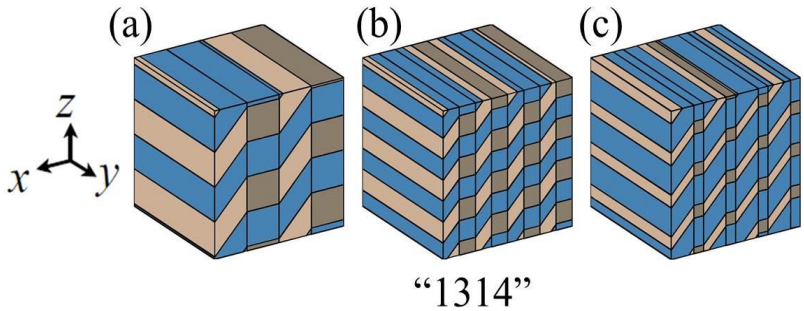

Fig. 3 Three equivalent twin patterns of "1314". The difference of (a) and (b) is their length scale; the difference of (b) and (c) is their volume fractions

All 616 sets of the microstructures should be checked whether the compatibility conditions (i)...(iii) are satisfied or not. Fig. 2 is an example of four laminate twin microstructures with the same variant permutation 1314 which satisfy the compatibility conditions (i)...(iii). In this way, all possible laminate twin microstructures can be obtained.

It is worth to mention that, since the present work focuses on the topology of twin patterns in the trigonal SMAs, the length scale of interface spacing of the microstructures generated here is irrelevant. Fig. 3 shows three equivalent twin patterns of "1314" with different length scale of interface spacing and different volume fraction of variants. It is worth noting that the current method is valid for bulk materials only. However, it is also ready to extend to analyze the microstructures in SMA films by taking the constraints due to the substrate into account. In general, the in-plane (11, 12, and 22) components of the overall strain state of the film are imposed by the corresponding substrate, and thus, only certain twin patterns are possible. However, in sufficiently thin films, only the in-plane compatibility conditions apply because a low energy elastic accommodation to out-of-plane incompatibilities is possible (Tsou 2010). Thus, some twin patterns which are not compatible in bulk materials, may be energetically favored in the films. These two factors lead subtleties for calculating all the possible twin patterns in SMA films. Thus, a further study is required and this issue will not be considered in the current work.

2.3 Numerical method based on nonlinear compatibility theory

Based on the methods discussed in Sec. 2.1 and Sec. 2.2, a complete microstructure database for the trigonal SMAs is obtained. In order to examine whether these microstructures are in a stable state, the nonlinearity should be taken into account. Here the numerical method developed in the authors' previous work is used (Tsou 2015). Consider a rank-1 twin laminate pattern, which is composed of a pair of pure variants (i, j). The two variants meet at an interface with unit normal vector n. A rigid rotation Q for the variant should be included in the non-linear compatibility equation

$$\mathbf{QU}_{(j)} - \mathbf{U}_{(i)} = \mathbf{b} \otimes \mathbf{n} \tag{4}$$

where b is an arbitrary vector; $U_{(i)}$ and $U_{(j)}$ are the transformation matrices of the trigonal variants (i, j).

In the present work, a $Ti_{50.3}Ni_{48.2}Fe_{1.5}$ SMA bulk material is used, where the crystal parameters

of parent phase are a_P=0.3019 nm, a_H=0.7355 nm and c_H=0.5283 nm in the hexagonal axes (Otsuka 2005). The transformation matrix of variant 1 can be obtained by the equation: $\mathbf{U}_{(1)} = \mathbf{R}_{(1)}\overline{\mathbf{U}}\,\mathbf{R}_{(1)}^{\mathrm{T}}$; $\mathbf{R}_{(1)}$ is a rotation matrix for variant 1 and the lattice transformation matrix in principle axis $\overline{\mathbf{U}}$ are written as

$$\mathbf{R}_{(1)} = \begin{pmatrix} 1/\sqrt{6} & 1/\sqrt{2} & 1/\sqrt{3} \\ -2/\sqrt{6} & 0 & 1/\sqrt{3} \\ 1/\sqrt{6} & -1/\sqrt{2} & 1/\sqrt{3} \end{pmatrix}, \ \overline{\mathbf{U}} = \begin{pmatrix} a_h/\sqrt{6}\,a_p & 0 & 0 \\ 0 & a_h/\sqrt{6}\,a_p & 0 \\ 0 & 0 & c_h/\sqrt{3}\,a_p \end{pmatrix} \tag{5}$$

Therefore, the lattice transformation matrix of variant 1 is

$$\mathbf{U}_{(1)} = \begin{pmatrix} 0.9998 & 0.0052 & 0.0052 \\ 0.0052 & 0.9998 & 0.0052 \\ 0.0052 & 0.0052 & 0.9998 \end{pmatrix} \tag{6}$$

The transformation matrix of the remaining crystal variants can be obtained by symmetry.

The interface normal n and rotation Q in Eq. (4) can be solved analytically (Bhattacharya 2003). This corresponds to rank-1 microstructures. Rank-2 twin patterns consisting of four regions of variants. Fig. 4 shows an example of a 2-dimensional view of a rank-2 “1314” laminate twin. The numbers of four regions followed the node number of tree diagram, so that Region 4 and 5 are separated by the interfaces with normal vector n_2; Region 4, 6 and Region 5, 7 are separated by the interface with normal vector n_1.

Based on the nonlinear theory, the four regions are required to joint perfectly around the junction, forming a ‘disclination-free’ rank-2 laminate twin pattern. The corresponding conditions can be written as follows

$$\begin{gathered} \mathbf{Q}_1\mathbf{U}_{(6)} - \mathbf{U}_{(4)} = \mathbf{b}_1 \otimes \mathbf{n}_1 \\ \mathbf{Q}_2\mathbf{U}_{(7)} - \mathbf{Q}_1\mathbf{U}_{(6)} = \mathbf{b}_2 \otimes \mathbf{n}_3 \\ \mathbf{Q}_1\mathbf{Q}_2\mathbf{Q}_3\mathbf{U}_{(5)} - \mathbf{Q}_1\mathbf{Q}_2\mathbf{U}_{(7)} = \mathbf{b}_3 \otimes \mathbf{n}_1 \\ \mathbf{U}_{(4)} - \mathbf{Q}_1\mathbf{Q}_2\mathbf{Q}_3\mathbf{U}_{(5)} = \mathbf{b}_4 \otimes \mathbf{n}_2 \\ \mathbf{n}_1, \mathbf{n}_2 \text{ and } \mathbf{n}_3 \text{ lie on a plane.} \end{gathered} \tag{7}$$

This only allows the formation of the patterns with the crystal variant permutation 1234. However, patterns such as “1314” and “1221” are still possible and observed in the present study.

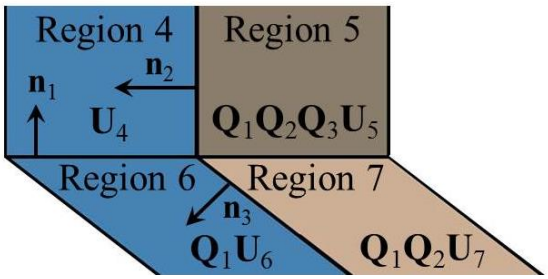

Fig. 4 A 2-dimensional view of a rank-2 “1314” laminate twin

Thus, here the nonlinear compatibility of the microstructures are solved numerically to seek an optimized solution. In order to solve the best fit rotation matrices Q_p (p=1...3) and vectors b_q (q=1...4), a mean square error method is used

$$\begin{aligned}\Gamma = \Big\{\sum_{j=1}^{3}\sum_{i=1}^{3}[&(b_{1_i}n_{1_j} - Q_{1_{ik}}U_{6_{kj}} + U_{4_{ij}})^2 \\ &+(b_{2_i}n_{3_j} - Q_{1_{ik}}Q_{2_{kl}}U_{7_{lj}} + Q_{1_{ik}}U_{6_{kj}})^2 \\ &+(b_{3_i}n_{1_j} - Q_{1_{ik}}Q_{2_{kl}}Q_{3_{lm}}U_{5_{mj}} + Q_{1_{ik}}Q_{2_{kl}}U_{7_{lj}})^2 \\ &+(b_{4_i}n_{2_j} - U_{4_{ij}} + Q_{1_{ik}}Q_{2_{kl}}Q_{3_{lm}}U_{5_{mj}})^2]\Big\}^{\frac{1}{2}}\end{aligned} \tag{8}$$

The error Γ of the solution represents the level of the defects in the microstructures. This also means that the error Γ can predict the likelihood of occurrence of laminate twin microstructures.

2.4 Specimen preparation and the procedure of pattern identification

The present model can be verified by comparing SEM images with microstructure database. The flow chart of the procedure for identifying twin patterns is shown in Fig. 5. The morphology of trigonal R-phase in the $Ti_{50.3}Ni_{48.2}Fe_{1.5}$ specimen was observed by SEM equipped with EBSD. A homogeneous $Ti_{50.3}Ni_{48.2}Fe_{1.5}$ ingot was hot-rolled to a 2 mm-thick plate at 1173 K. The trigonal R-phase start temperature was 33°C which determined by differential scanning calorimetry (DSC) with a heating rate of 10 K/min. The specimen was gradually ground with 400#, 800#, and 1000# emery papers and electropolished at 12 V with an electrolyte consisting of 10% H_2SO_4 and 90% CH_3OH in volume at room temperature. The kikuchi patterns of the specimen was scanned by FEI Nova 450 SEM equipped with an EDAX^{TM} Hikari XP EBSD Camera. The orientation of the grains was analyzed by the software, Orientation Imaging Microscopy (OIM^{TM}). A forward scatter detector was chosen to take the morphologies of the specimen. The crystallographic orientation of observation plane was specified by Euler angles.

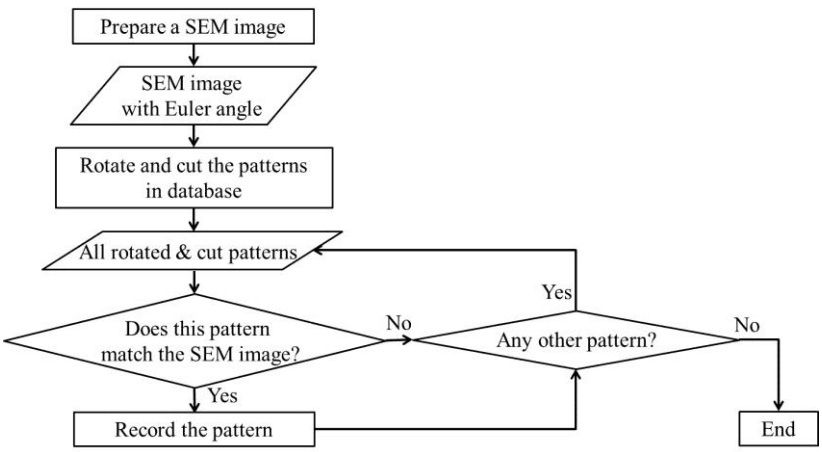

Fig. 5 The flow chart of the iteration procedure for identifying twin patterns

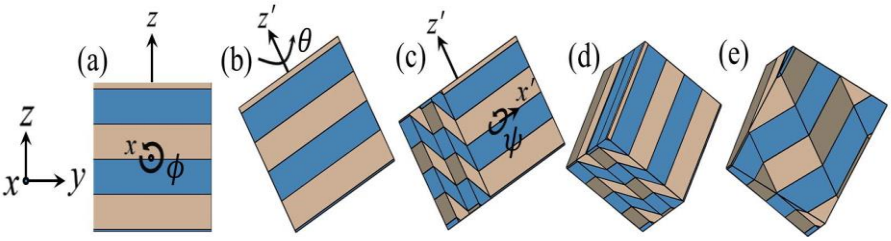

Fig. 6 An example of how to rotate and cut the microstructure "1314"

In order to compare SEM images with laminate twin microstructures, the patterns in the microstructure database need to be rotated and cut to get the correct observation plane according to the Euler angles. There are three angles (ϕ, θ, Ψ) in Euler angles. Fig. 6 is an example of the procedure of rotating and cutting the pattern "1314". Firstly, the pattern is rotated the *z*-axis about *x*-axis by ϕ and the rotated *z*-axis is defined as a new axis *z'*. It is then rotated about *z'*-axis by θ and, similarly, the *x*-axis becomes *x'*-axis. Next, it is rotated about *x'*-axis by Ψ, as shown in Fig. 6(d). Finally, the observation plane can be obtained by cutting the rotated pattern from the centroid. In this way, all the rotated and cut patterns in the microstructure database can be compared with the SEM image one by one. Note that multiple solutions for observed topology are possible, thus, whenever the pattern matches the observation, the patterns should be recorded. Once all patterns have been compared and there are more than one matched patterns found, the topology in the SEM image is identified.

3. Numerical and experiment results of laminate twin patterns

Many types of pattern are observed in the SEM images, such as the well-known classic herringbone pattern and other patterns, such as non-classic herringbone, toothbrush and checkerboard. These patterns are also identified by the current model. Classic herringbone patterns are the most commonly observed patterns in the trigonal R-phase SMAs. It typically consists of four different trigonal crystal variants and its interfaces contain the rank-1 interfaces with normal vector $<1\ 1\ 0>_p$ and the rank-2 interfaces with normal vector $<1\ 0\ 0>_p$. Where the subscript *p* indicates that the normals are indexed with the coordinate of parent phase. Fig. 7 shows six examples of the classic herringbone with different patterns on the observation plane, and the corresponding results of identification are attached. According to the interface orientation in the observed patterns, the pattern with the same interface orientation in the microstructure database can then be found. Note that the volume fraction of the crystal variants in the patterns is irrelevant as mentioned above. The classic herringbone patterns "1324", "1234" and "1342" are now examined by the nonlinear compatibility numerical model mentioned in Sec. 2.3. Surprisingly, they all have the error $\Gamma = 0$. This indicates that classic herringbone is a disclination-free rank-2 laminate microstructure. Thus, it is the reason why they can be frequently observed in the SMA crystals.

Non-classic herringbone patterns (Tsou 2015) are also found in the current work. Their interfaces contain the rank-1 interfaces with normal vector $<1\ 0\ 0>_p$ and the rank-2 interfaces with normal vector $<1\ 1\ 0>_p$. Fig. 8 shows four examples of non-classic herringbone. It is interesting to note that Fig. 8(a), (b) are the same patterns "1343", and however, their appearances are different

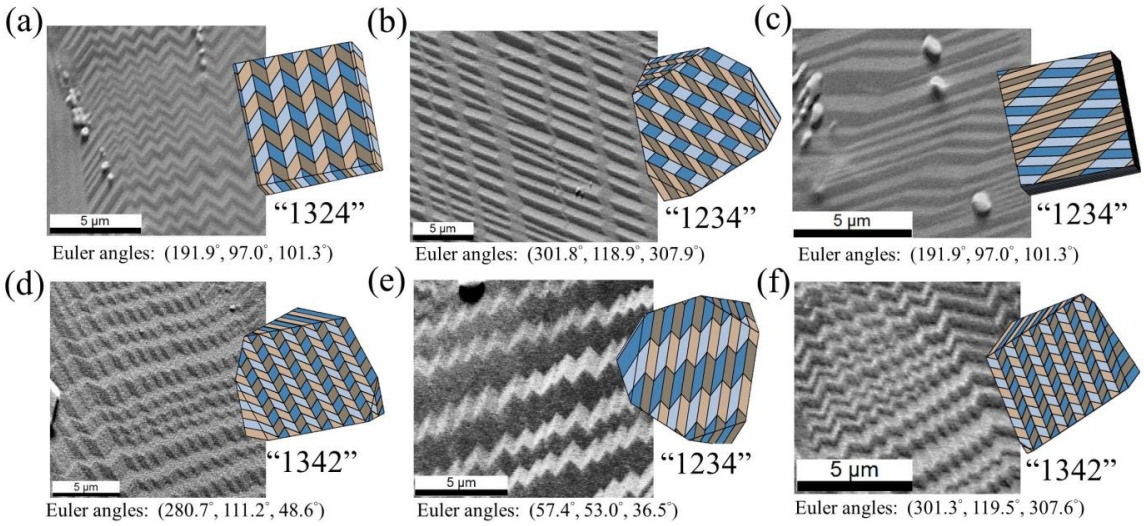

Fig. 7 Six examples of classic herringbone with different patterns on the observation plane, and the corresponding results of identification

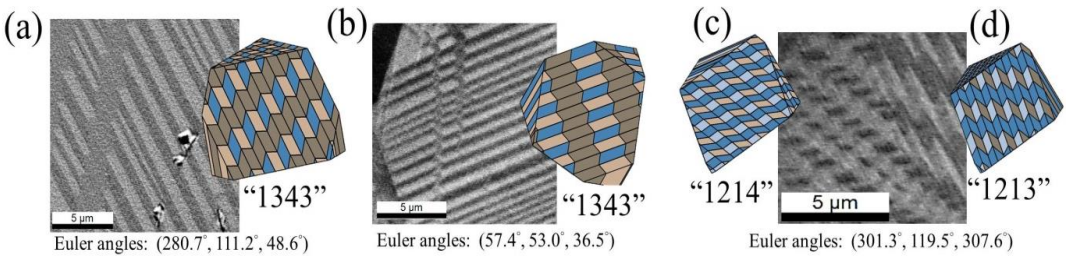

Fig. 8 Four examples of non-classic herringbone pattern and the corresponding results of identification

due to the different Euler angles. This shows that the power of the current model, which can give a precise identification of the observed microstructures. Fig. 8(c), (d) contain both "1213" and "1214" patterns separated by an incompatible interface in one grain. The Γ value of the patterns "1343", "1213" and "1214" are determined by nonlinear compatibility theory, giving $\Gamma = 0.0103$. This indicates that the non-classic herringbone patterns typically have minor defect of disclination, i.e., at a relatively high energy state comparing to the classic herringbone patterns. The non-classic herringbone patterns cannot satisfy Eq. (7), but their existence is still possible. In the present work, we found four cases of the non-classic herringbone patterns in the specimen.

Another possible microstructure is the toothbrush pattern (Tsou 2015). We found four examples, "2332", "1441", and "2442", as shown in Fig. 9. They all have the nonlinear compatibility error $\Gamma = 0.0147$, which is slightly greater than it of the non-classic herringbone patterns. Thus, the likelihood of the observation of toothbrush is expected to be similar to it of the non-classic herringbone patterns. It is interesting to note that the toothbrush pattern in Fig. 9(d) has needle-like shape, which looks different to the stripe-like pattern with constant thickness predicted by the current model. We suspect that the pattern in the specimen ran out of the available energy during the middle of the martensitic transformation process, and even the pattern consists incompatible interfaces near the needle tips. The pattern requires further external loading to

overcome the energy barrier of the switching and to continue such kinetic process. However, the current model is purely kinematic in nature. The nucleation of new regions of variant and the route along which the microstructure evolves were not yet captured.

Fig. 10 is the only observed result of checkerboard pattern "1243". It is interesting noting that, similar to the classic herringbone pattern, the checkerboard pattern (Tsou 2015) also consists of all four trigonal crystal variants. However, the checkerboard pattern has $\Gamma = 0.0206$, and cannot have a disclination-free topology. Thus, the probability of the observation of the checkerboard pattern is relatively lower than the classic herringbone and other patterns.

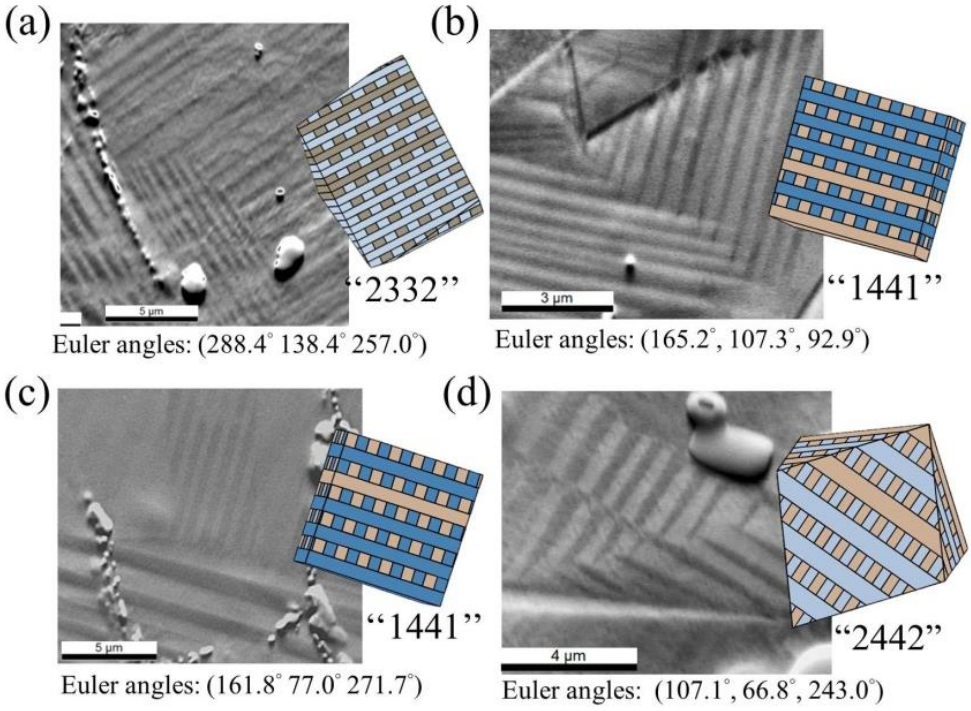

Fig. 9 Four examples of toothbrush pattern and the corresponding results of identification

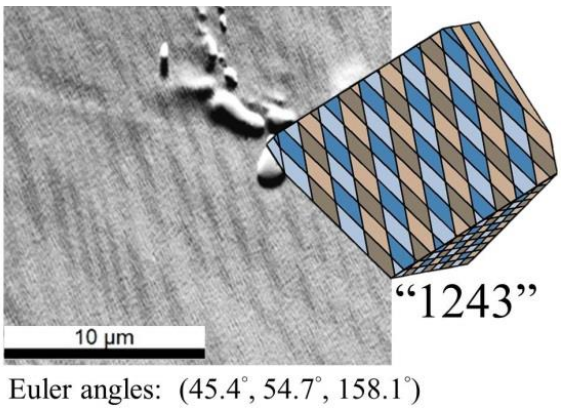

Fig. 10 An example of checkerboard pattern and the corresponding result of identification

4. Conclusions

In the present work, a numerical model combining linear and nonlinear compatibility theories are developed. It is then applied to construct the microstructure database for the trigonal SMAs. A procedure, which processes the patterns in the microstructure database and matches them with the patterns observed in the experiments, is also specified. Then, the model and the microstructure database are validated by using the SEM images and the crystallographical axes obtained by EBSD. Many microstructures are observed and identified, by matching the interface orientations. The results show that it is common to find the classic herringbone patterns in the specimens. However, some other interesting trigonal R-phase patterns, such as non-classic herringbone, toothbrush and checkerboard, are also discovered. The level of the incompatibility in the microstructure, Γ, developed by nonlinear compatibility is determined for all the observed patterns. The lower value the Γ is, the more frequent the corresponding microstructure can be found. This statement agrees with our observation. The present work provides a method to realize the overview of laminate twin microstructures. The procedure is rapid and efficient which can be extended to other crystal systems and materials.

Acknowledgments

The authors wish to acknowledge the support of Ministry of Science and Technology (MOST) Taiwan, Grant No. MOST 102-2218-E-009-019-MY2, and thank Chih-Hsuan Chen for preparing the specimen and taking SEM images.

References

Ball, J.M. and James, R.D. (1989), *Fine Phase Mixtures as Minimizers of Energy Analysis and Continuum Mechanics*, Springer.

Bhattacharya, K. (2003), *Microstructure of Martensite: Why it Forms and How it Gives Rise to the Shape-Memory Effect*, **2**, Oxford University Press.

Fan, G., Zhou, Y., Otsuka, K. and Ren, X. (2006), "Ultrahigh damping in R-phase state of Ti-Ni-Fe alloy", *Appl. Phys. Lett.*, **89**(16), 161902.

Goldsztein, G.H. (2001), "The effective energy and laminated microstructures in martensitic phase transformations", *J. Mech. Phys. Sol.*, **49**(4), 899-925.

Hane, K.F. and Shield, T. (1999), "Microstructure in the cubic to monoclinic transition in titanium-nickel shape memory alloys", *Acta Mater.*, **47**(9), 2603-2617.

Hane, K.F. and Shield, T.W. (2000), "Microstructure in a cubic to orthorhombic transition", *J. Elast. Phys. Sci. Sol.*, **59**(1-3), 267-318.

Kastner, O., Eggeler, G., Weiss, W. and Ackland, G.J. (2011), "Molecular dynamics simulation study of microstructure evolution during cyclic martensitic transformations", *J. Mech. Phys. Sol.*, **59**(9), 1888-1908.

Levitas, V.I., Idesman, A.V. and Preston, D.L. (2004), "Microscale simulation of martensitic microstructure evolution", *Phys. Rev. Lett.*, **93**(10), 105701.

Miyazaki, S. and Ishida, A. (1999), "Martensitic transformation and shape memory behavior in sputter-deposited TiNi-base thin films", *Mater. Sci. Eng.: A*, **273**, 106-133.

Murakami, Y., Ohba, T., Morii, K., Aoki, S. and Otsuka, K. (2007), "Crystallography of stress-induced (trigonal) martensitic transformation in Au-49.5 at.% Cd alloy", *Acta Mater.*, **55**(9), 3203-3211.

Otsuka, K. and Ren, X. (2005), "Physical metallurgy of Ti-Ni-based shape memory alloys", *Prog. Mater. Sci.*, **50**(5), 511-678.

Roytburd, A., Kim, T., Su, Q., Slutsker, J. and Wuttig, M. (1998), "Martensitic transformation in constrained films", *Acta Mater.*, **46**(14), 5095-5107.

Shu, Y. and Yen, J. (2007), "Pattern formation in martensitic thin films", *Appl. Phys. Lett.*, **91**(2), 021908.

Shu, Y. and Yen, J. (2008), "Multivariant model of martensitic microstructure in thin films", *Acta Mater.*, **56**(15), 3969-3981.

Tomozawa, M., Kim, H.Y. and Miyazaki, S. (2006), "Microactuators using R-phase transformation of sputter-deposited Ti-47.3 Ni shape memory alloy thin films", *J. Intellig. Mater. Syst. Struct.*, **17**(12), 1049-1058.

Tsou, C. and Huber, J. (2010), "Compatible domain arrangements and poling ability in oriented ferroelectric films", *Contin. Mech. Thermodyn.*, **22**, 203-219.

Tsou, C. and Huber, J. (2010), "Compatible domain structures and the poling of single crystal ferroelectrics", *Mech. Mater.*, **42**(7), 740-753.

Tsou, C.H., Chen, C.S. and Wu, S.K. (2015), "Classification and analysis of trigonal martensite laminate twins in shape memory alloys", *Acta Mater.*, **89**, 193-204.

Tsou, H.J. and Shu, Y. (2012), "A sharp interface model of compatible twin patterns in shape memory alloys", *Smart Mater. Struct.*, **21**(9), 094010.

Wu, P., Ma, X., Zhang, J. and Chen, L. (2008), "Phase-field simulations of stress-strain behavior in ferromagnetic shape memory alloy Ni 2 MnGa", *J. Appl. Phys.*, **104**(7), 073906.

Zhang, J. and Chen, L. (2005), "Phase-field model for ferromagnetic shape-memory alloys", *Philosoph. Mag. Lett.*, **85**(10), 533-541.

Zhong, Y., Gall, K. and Zhu, T. (2012), "Atomistic characterization of pseudoelasticity and shape memory in NiTi nanopillars", *Acta Mater.*, **60**(18), 6301-6311.

DC